

## A Numerical Study of the Air Flow Over Mountains Using the Two-Dimensional Version of the University of Virginia Mesoscale Model

YTZHAQ MAHRER AND ROGER A. PIELKE

*Department of Environmental Sciences, University of Virginia, Charlottesville 22903*

(Manuscript received 23 May 1975, in revised form 11 August 1975)

### ABSTRACT

The two-dimensional version of the University of Virginia mesoscale model has been adopted to study the air flow over a mountain using a terrain-following coordinate system. Some improvements in the boundary layer parameterization have been incorporated into the model according to a technique suggested by Deardorff. Two sets of experiments are studied. In the first one, the model is integrated to a steady-state solution under different initial velocity fields. In the second experiment, a diurnal temperature wave is imposed on the surface so that a pressure gradient is developed between the sloping terrain and the surrounding atmosphere. Results are compared against other mountain numerical models and against existing observations.

### 1. Introduction

In previous studies of air flow over mountains, both linear and nonlinear models were developed. One of the first linear models was presented by Queney (1948), who was able to obtain some of the observed features of air flow over mountains. Scorer (1949) applied Queney's equation to separated layers characterized by different critical wavelengths. Following Scorer (1949), Corby and Sawyer (1958), Sawyer (1960) and others solved the equations in multi-layered models. In more recent years, several papers have dealt with the linear theory of air flow over a mountain with an arbitrary basic flow (e.g., Wallington, 1970; Vergeiner, 1971). Time-dependent, nonlinear numerical calculations have been demonstrated by Hovermale (1965), Foldvik and Wurtele (1967), Deaven (1974), and Anthes and Warner (1974). The latter investigators have carried out some experiments with different upper-pressure surfaces. Their calculations show similar results in the lower troposphere (below 500 mb) for experiments with top-pressure surfaces of 0, 200, 400, and even 500 mb.

### 2. Basic equations

The model presented in this paper uses a boundary-layer formulation where both the surface layer and the planetary boundary layer may vary with time as discussed in detail by Pielke and Mahrer (1975). Encouraged by Anthes and Warner's results, and since our main interest was the lower troposphere, the model's upper boundary was put initially at 10 km (276 mb). The purpose of this paper is to discuss the numerical simulation of air flow over a mountain with

and without diurnal heating cycles, and to compare the results qualitatively against existing observations.

The two-dimensional version of the University of Virginia mesoscale model<sup>1</sup> has been adopted for this study. The development of this model is an intermediate step in the incorporation of topographic effects into the three-dimensional mesoscale model discussed by Pielke (1974a). As shown by Pielke (1974b), a two-dimensional mesoscale model can be used to investigate the properties of atmospheric circulations even though spatial variation of the dependent variables in the third direction is ignored. The basic equations in the Cartesian coordinate system are transformed into a terrain-following coordinate system  $(x, y, z^*, t)$  by the transformation  $z^* = \bar{s}(z - z_G)/(s - z_G)$ , where  $\bar{s}$  is the initial height of the top of the model,  $s$  the material surface top of the model (initially  $s = \bar{s}$ ), and  $z_G$  the ground elevation.

The equations of motion, potential temperature, and continuity for hydrostatic flow, using the above transformation, are given below (symbols defined in the Appendix):

$$\frac{du}{dt} = f v - \theta \frac{\partial \pi}{\partial x} + g \frac{z^* - \bar{s}}{\bar{s}} \frac{\partial z_G}{\partial x} - g \frac{z^*}{\bar{s}} \frac{\partial s}{\partial x} + \left( \frac{\bar{s}}{s - z_G} \right)^2 \frac{\partial}{\partial z^*} \left( K_z^m \frac{\partial u}{\partial z^*} \right), \quad (1)$$

$$\frac{dv}{dt} = -f u + f U_G + \left( \frac{\bar{s}}{s - z_G} \right)^2 \frac{\partial}{\partial z^*} \left( K_z^m \frac{\partial v}{\partial z^*} \right), \quad (2)$$

<sup>1</sup> The University of Virginia model is an improved version of the model discussed by Pielke (1974a). The paper by Pielke and Mahrer (1975) discusses some of the improvements.

$$\frac{d\theta}{dt} = \left( \frac{\bar{s}}{s-z_G} \right)^2 \frac{\partial}{\partial z^*} \left( K_z^\theta \frac{\partial \theta}{\partial z^*} \right), \quad (3)$$

$$\frac{\partial u}{\partial x} + \frac{\partial w^*}{\partial z^*} - \frac{u}{s-z_G} \frac{\partial z_G}{\partial x} + \frac{1}{s-z_G} \left( \frac{\partial s}{\partial t} + u \frac{\partial s}{\partial x} \right) = 0, \quad (4)$$

$$\frac{\partial \pi}{\partial z^*} = - \frac{s-z_G}{\bar{s}} \frac{g}{\theta}, \quad (5)$$

where

$$\pi = C_p \left( \frac{P}{P_{00}} \right)^{R/C_p},$$

$$w^* = \frac{\bar{s}}{s-z_G} w - \frac{z^*}{s-z_G} \left( \frac{\partial s}{\partial t} + u \frac{\partial s}{\partial x} \right) + \frac{z^* - \bar{s}}{s-z_G} \frac{\partial z_G}{\partial x}, \quad (6)$$

$$\frac{d}{dt} = \frac{\partial}{\partial t} + u \frac{\partial}{\partial x} + w^* \frac{\partial}{\partial z^*}. \quad (7)$$

A prognostic equation for the free surface can be obtained by integrating (4) from  $z^*=0$  to  $z^*=\bar{s}$  with the boundary condition  $w^*=0$  on both surfaces. The resultant equation is given by

$$\frac{\partial s}{\partial t} = - \frac{1}{\bar{s}} \int_0^{\bar{s}} \frac{\partial}{\partial x} [u(s-z_G)] dz^*. \quad (8)$$

### 3. Boundary layer formulations

The vertical exchange coefficients in the surface layer are given by

$$K_z^{(m)}(z^*) = k_0 u_* z^* / [\phi_i(|\xi|)],$$

$$K_z^{(\theta)}(z^*) = \beta K_z^{(m)}(z^*),$$

where the subscript  $i=1$  denotes unstable stratification in the surface layer, and  $i=2$  stable stratification. This formulation is rigorously valid only for horizontally homogeneous terrain, but will be used over mountainous terrain for lack of an alternate theoretical expression for turbulent fluxes over horizontally heterogeneous terrain. The nondimensional stability length  $\xi$  and the parameter  $\beta$  are defined as

$$|\xi| = z^* / |L_*|,$$

$$\beta = \begin{cases} [\phi_1(|\xi|)]^{-1}, & i=1 \\ 1, & i=2 \end{cases}$$

where

$$L_* = -\bar{\theta} u_*^2 / (\sigma k_0 g \theta_*).$$

The exchange coefficients above the surface layer are determined using the method discussed by O'Brien (1970), while the technique to determine the top of the planetary boundary layer is based on the work of Deardorff (1974). In Deardorff's technique, the boundary layer grows as a function of surface heat and mo-

mentum fluxes, mesoscale vertical motion, and the overlying thermodynamic stability, and is given by

$$\frac{\partial z_i}{\partial t} = -u \frac{\partial z_i}{\partial x} + w_i^* + \frac{1.8[(W_*^3 + 1.1u_*^3 - 3.3u_*^2 f z_i)]}{g \frac{z_i^2}{\theta_*} \frac{\partial \theta^+}{\partial z} + 9W_*^2 + 7.2u_*^2}. \quad (9)$$

The value of  $W_*$  is given as

$$W_* = \begin{cases} [(-g/\theta_*) u_* \theta_* z_i]^{\frac{1}{3}}, & \theta_* \leq 0 \\ 0, & \theta_* > 0 \end{cases}$$

For more information regarding the parameterization of the boundary layer, see Pielke (1974a) and Pielke and Mahrer (1975).

### 4. Initial and boundary condition

To avoid numerical integration problems arising from the initial accelerations, we followed Deaven's (1974) procedure of "diastrophism," that is, the mountain is allowed to grow during the first two hours, from an initial horizontal surface up to its maximum height. The initial condition for  $t \leq 0$  are

$$\left. \begin{aligned} P(z=z^*=0) &= 1013 \text{ mb} \\ T(z=z^*=0) &= 25^\circ\text{C} \\ T(z) &= T(z=0) - 6.5 \times 10^{-5} z \end{aligned} \right\}$$

Over the flat surface at the initial time, the shear stress, the Coriolis and the pressure gradient forces are assumed in balance as expressed by

$$\frac{\partial}{\partial z} \left( K_z^{(m)} \frac{\partial u}{\partial z} \right) + f(v - V_g) = 0, \quad (10)$$

$$\frac{\partial}{\partial z} \left( K_z^{(m)} \frac{\partial v}{\partial z} \right) + f(U_g - u) = 0. \quad (11)$$

The initial wind profile in the planetary boundary layer is calculated from (10) and (11) by an iterative method. Above the planetary boundary layer the velocities are assumed to be geostrophic.

The boundary condition at  $z^*=0$  are given by

$$u = v = w^* = 0 \quad \text{and} \quad \theta = \theta(t),$$

while

$$\left. \begin{aligned} \frac{\partial u}{\partial z^*} = \frac{\partial v}{\partial z^*} = w^* &= 0 \\ \pi &= \pi(\bar{s}) - g(s - \bar{s}) / \theta(s) \\ \frac{\partial \theta}{\partial z} &= 0.4^\circ\text{C} / (100 \text{ m})^{-1} \end{aligned} \right\}$$

on  $z^* = \bar{s} = 10 \text{ km}$ .

At the lateral boundaries,  $x = \pm L$ ,

$$w^* = - \frac{\partial}{\partial x} (u, v, \theta, \pi, s) = 0.$$

TABLE 1. Horizontal distances (km) from center of mountain at each model grid point.\*

Grid points	17	18	19	20	21	22	23	24	25
		16	15	14	13	12	11	10	9
Distance from center	0	± 10.0	± 20.1	± 30.5	± 41.3	± 52.6	± 64.7	± 77.9	± 92.8
Grid points	26	27	28	29	30	31	32	33	0
	8	7	6	5	4	3	2	1	
Distance from center	± 109.9	± 130.7	± 157.9	± 199.0	± 286.7	± 675.37	± 1237.4	± 1800	

\* + signs for grid points to the right side of the mountain, - signs to the left.

A roughness parameter of  $z_0=0.04$  m was used in all the experiments.

### 5. Numerical aspects

The numerical integration of (1)–(3) and (8), with the initial and boundary conditions given above, were computed by forward differences in time with upwind differences in space for the advective terms. The remainder of the terms except for the vertical flux term were determined by centered differences. The vertical eddy transport terms were evaluated by a DuFort and Frankel difference scheme (Richtmyer, 1957) in order to avoid the time-step restriction required by Pielke (1974a) arising from those terms, especially during the heating cycle. The numerical form for those terms is given by

$$\frac{\partial}{\partial z^*} K \frac{\partial u}{\partial z^*} = \frac{K_{i,j+\frac{1}{2}} \frac{u_{i,j+1}^n - u_{i,j}^{n+1}}{z^*(j+1) - z^*(j)} - K_{i,j-\frac{1}{2}} \frac{u_{i,j}^{n+1} - u_{i,j-1}^n}{z^*(j) - z^*(j-1)}}{z^*(j+\frac{1}{2}) - z^*(j-\frac{1}{2})}, \quad (12)$$

where  $n$  denotes the time step.

A full description of the numerical procedure including the staggered grid used was given in Pielke (1974a).

In order to minimize lateral boundary effects, stretching is applied symmetrically about the center of the mountain. Schulman (1970) defined a stretching function given by

$$f(x) = c \left[ ax + \tanh \left( \frac{x - x_0}{\sigma_0} + b \right) \right],$$

where  $b = \tanh(x_0/\sigma_0)$ ,  $x_0 = 0.5$ ,  $a = 0.5$ , and

$$c = [a + b + \tanh(1 - x_0/\sigma_0)]^{-1}.$$

For the purpose of this study, we chose a minimum  $\Delta x$  of 10 km with a model width of 3600 km. The corresponding value of  $\sigma_0$  with 33 horizontal grid points is 0.036. The maximum  $\Delta x$  is 562 km at the lateral boundaries. The horizontal distances from the center of the mountain at each grid point are listed in Table 1.

In the vertical, the atmosphere was divided into 12 levels with heights of 0, 50, 100, 1200, 1800, 2400, 3600, 4800, 6000, 7200, 8400 and 10 000 m at which  $u$ ,  $v$ ,  $\rho$  and  $w^*$  are computed, while  $\theta$  is at intermediate heights. The time step in the integration was 2 min, except for experiment B, where a time step of 1 min was required for linear stability.

The function chosen to represent the height of the mountain was

$$z_G = H_0 B^2 / (x^2 + B^2),$$

which roughly represents the average topography near Boulder, Colo., with  $H_0 = 1.9$  km and  $B = 15$  km (Deaven, 1974).

### 6. Horizontal exchange coefficients

Two forms of horizontal smoothing were tested. In the first, a horizontal exchange coefficient of the form

$$K_H = \alpha (\Delta x)^2 \left[ \left( \frac{\partial v}{\partial x} \right)^2 + \frac{1}{2} \left( \frac{\partial u}{\partial x} \right)^2 \right]^{\frac{1}{2}} \quad (13)$$

(where  $\alpha$  is a numerical constant) was applied to the  $u$ ,  $v$ ,  $\theta$  fields. The second, proposed by Shuman (1957), was a horizontal smoother applied to the  $u$  and  $v$  fields. If  $\phi$  is the field to be smoothed, then the smoothed value  $\bar{\phi}$  is

$$\bar{\phi}_i = (1 - s_i) \phi_i + s_i \frac{\phi_{i+1} + \phi_{i-1}}{2}, \quad (14)$$

where  $0.01 \leq s_i < 0.5$ . The value of  $s_i$  has been set equal to 0.5 on the lateral boundaries and decreases linearly to its lowest value of 0.01 at 10 grid points from the center. Experiments with these two forms have been performed and it was found that by smoothing the  $u$  and  $v$  fields according to (14), a steady-state solution was obtained after 4 h, while with the horizontal exchange-coefficient method, a steady-state solution was achieved only after 8 h with almost the same results. Therefore, we have adopted the numerical smoothing technique, rather than the horizontal exchange coefficient form.

### 7. Results

In this section, the results with and without heating of the surface are compared against Hovermale's (1965)

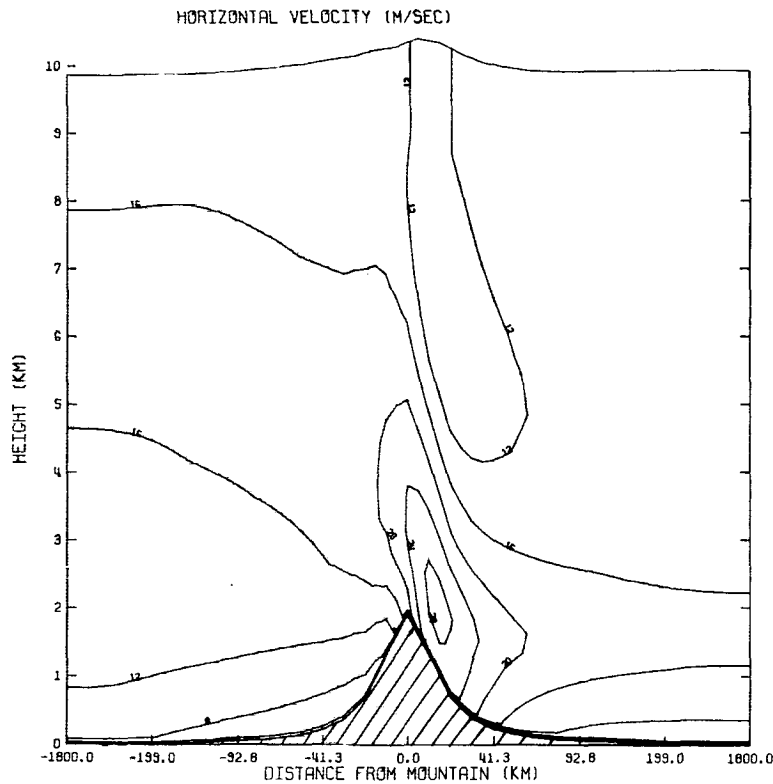


FIG. 1. East-west velocity component 4 h after the mountain was introduced. (The line at the top in this and corresponding figures corresponds to the heights of the material surface.)

and Deaven's (1974) numerical models and against observational data collected during the 1970 Colorado Lee Wave Program.

a. Without heating

The initial conditions for this experiment are identical to those used by Deaven (1974), i.e.,  $\partial T/\partial z = 0.0065^\circ\text{C m}^{-1}$  and  $U_0 = 15 \text{ m s}^{-1}$ , except in the planetary boundary layer where a balance solution is obtained for the initially flat surface as mentioned in Section 4.

1) HORIZONTAL VELOCITY

Fig. 1 shows the distribution of the east-west component of the horizontal velocity after 4 h of integration (4 h after the mountain reached its maximum height). The increase of the wind in the lee of the mountain and the decrease on the windward side are apparent. The maximum velocity is found to be at an elevation of about 400 m above the ground with a value of  $28 \text{ m s}^{-1}$  rather than on the surface as found in Deaven's and Hovermale's results. This is a result of our boundary layer formulation since ground friction is included more realistically. A minimum of  $4 \text{ m s}^{-1}$  and a maximum of  $21 \text{ m s}^{-1}$  are observed at the first grid level on the windward and lee slopes respectively. The vertical

profiles of the east-west wind component on the lee slope for three different initial velocity fields ( $5, 10$  and  $15 \text{ m s}^{-1}$ ) are shown in Fig. 2 and agree quite well with the critical vertical wavelength predicted from linear theory which is defined as

$$L = 2\pi/K_c,$$

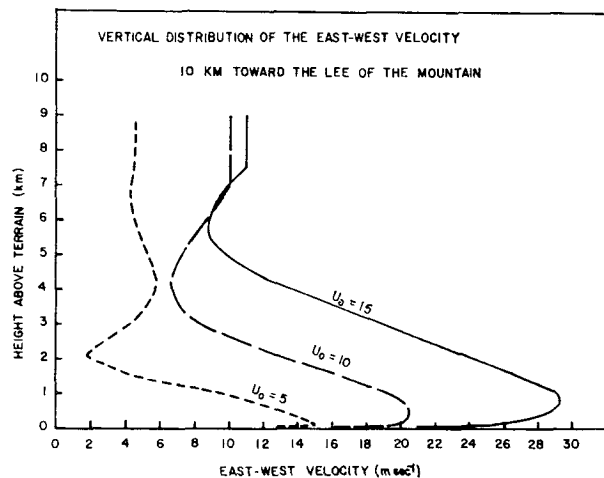


FIG. 2. Vertical profiles of the east-west wind velocity component on the lee slope for three different initial velocity fields ( $5, 10$  and  $15 \text{ m s}^{-1}$ ).

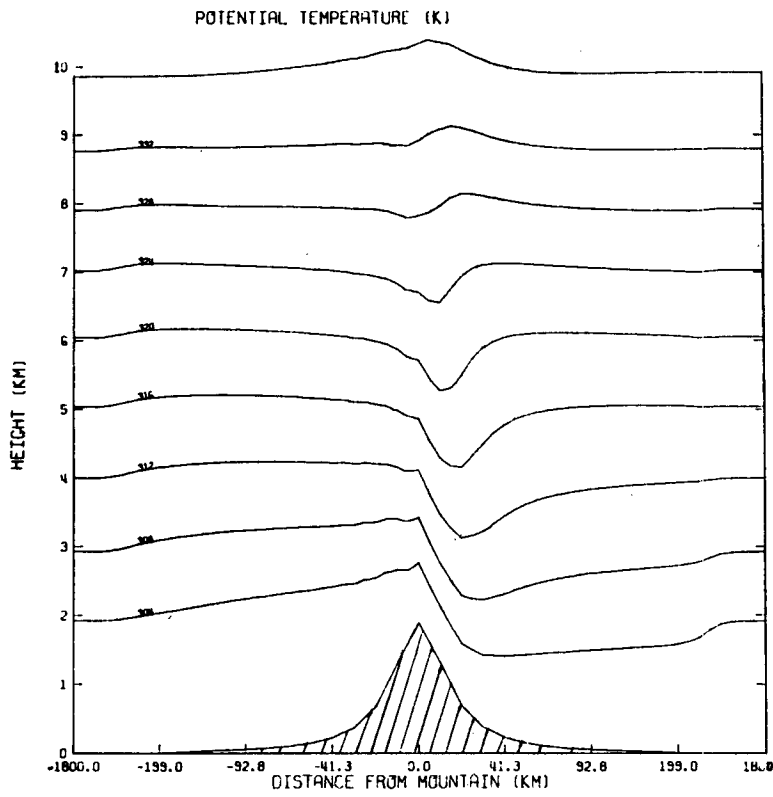


FIG. 3. Potential temperature distribution 4 h after the mountain was introduced.

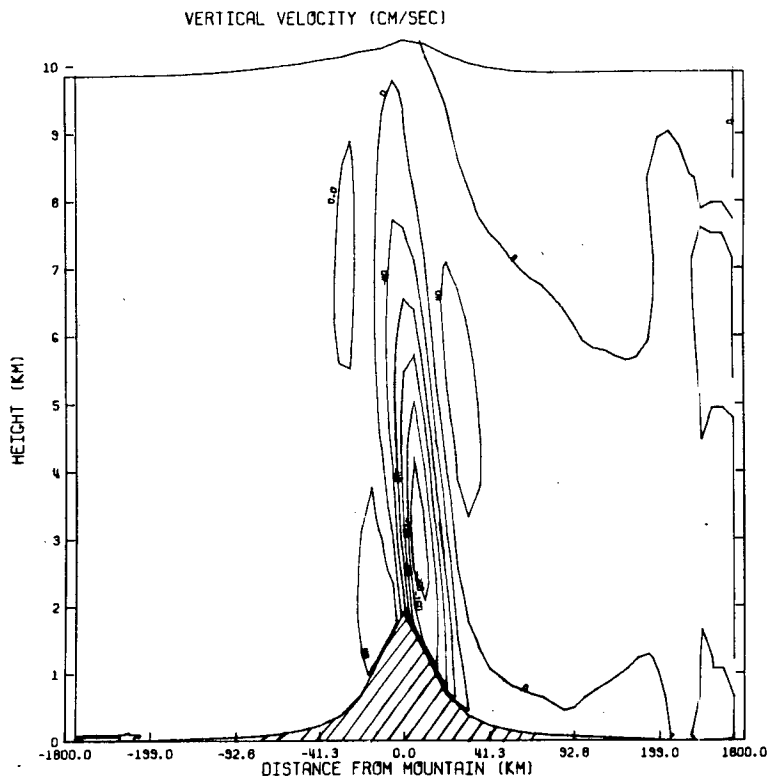


FIG. 4. Vertical velocity field 4 h after the mountain was introduced.

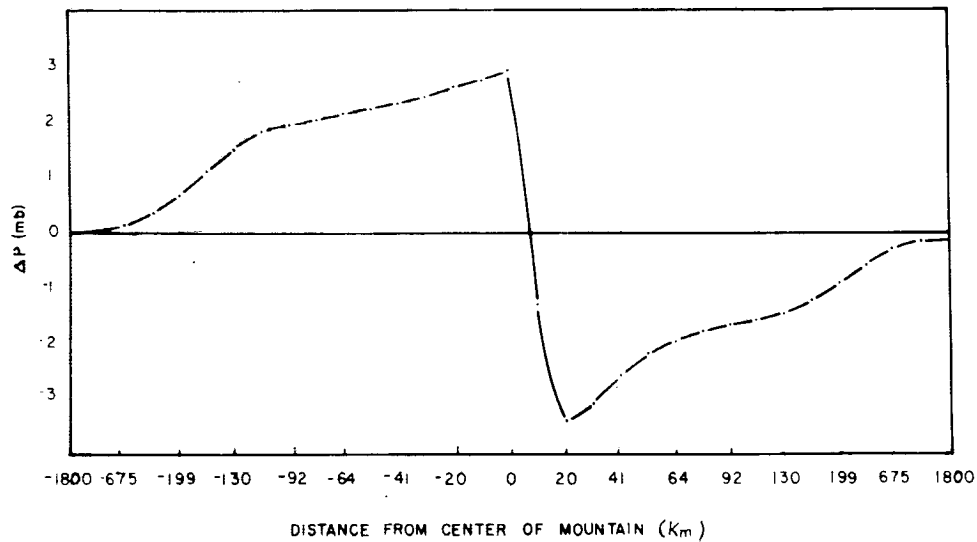


FIG. 5. Perturbation pressure at the ground.

where

$$K_0^2 = \frac{g(\partial\theta/\partial z)}{\theta U^2}.$$

The formula was derived by Scorer (1949) and Queney (1948) from their frictionless, linear mountain models. The vertical wavelengths from our results are 3.6, 6.4 and 8.8 km for  $U_0 = 5, 10$  and  $15 \text{ m s}^{-1}$  respectively, while the corresponding theoretical wavelengths are 3.1, 6.2 and 9.3 km.

## 2. POTENTIAL TEMPERATURE

The potential temperature distribution (Fig. 3) has a temperature minimum produced by the orographic lifting with the lowest values at the mountain divide and a maximum produced by sinking on the lee side. Both the minimum and the maximum in potential temperature tilt upstream with increasing elevation. The temperature on the lee side at an elevation of 660 m above the ground is about  $3^\circ\text{C}$  higher than on the windward side.

## 3) VERTICAL VELOCITY

The vertical velocity fields (Fig. 4) have significant upward components on the windward slope with a maximum of  $0.7 \text{ m s}^{-1}$  while the motion is downward on the lee slope with a maximum speed of  $2.2 \text{ m s}^{-1}$ . Deaven's results show a maximum downward component of  $2.4 \text{ m s}^{-1}$  at about the same location, but a smaller upward component on the windward side ( $<0.4 \text{ m s}^{-1}$ ). It should be noted that foehn clouds, due to upward motion of the windward side, were observed by Ludlam (1952) in the United Kingdom over the Chilterns, and in the vicinity of the Rocky Mountains by Danielson and Bleck (1970), under strong wind-flow regimes.

## 4) PRESSURE

FIG. 5 shows the perturbation pressure at the ground where there is a maximum of 2.9 mb near the crest and a minimum of  $-3.4 \text{ mb}$  on the lee slope. This pressure distribution is consistent with the strong convergence and divergence fields over the windward and lee slopes respectively. A pressure minimum is often observed under strong foehn wind conditions on the lee of the Rocky Mountains. A pressure dip of 5-7 mb was observed on the eastern slope by Lilly and Zipser (1972).

### b. Experiment with vertical wind shear

In the following experiment a vertical wind shear of  $4.5 \text{ m s}^{-1} \text{ km}^{-1}$  is modeled above the planetary boundary layer; otherwise the initial conditions are the same as in the preceding experiment. As before, the equations are integrated to a steady-state solution.

## 1) POTENTIAL TEMPERATURE

In the lower levels up to 4 km (Fig. 6) the isentropic surfaces follow the bell-shaped mountain with less amplitude than in the previous experiment. They are warped upward on the windward side, suggesting a foehn cloud as mentioned before. At higher elevations, the isentropes are deflected downward as they approach the ridge barrier, then plunge down as they pass over the crest. Between 4 and 8 km the elevations of the isentropes to the lee of the mountain are lower than or equal to the elevations on the windward side, while above 8 km the isentropes ascend to higher elevations on the lee side. The greatest uplift occurs where we have a cell of upward motion (Fig. 7) and one would expect to find a cirrus cloud shield there if the air is moist. Cirrus cloud shields were, in fact, observed for similar wind conditions at an elevation of 12 km in the

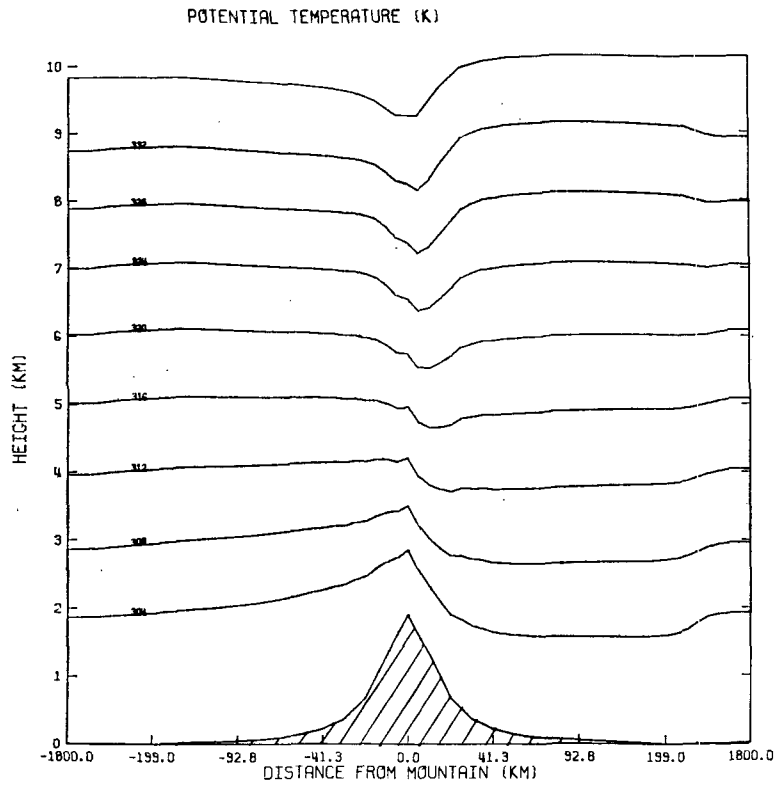


FIG. 6. As in Fig. 3 but with an initial vertical shear of the horizontal wind above the planetary boundary layer.

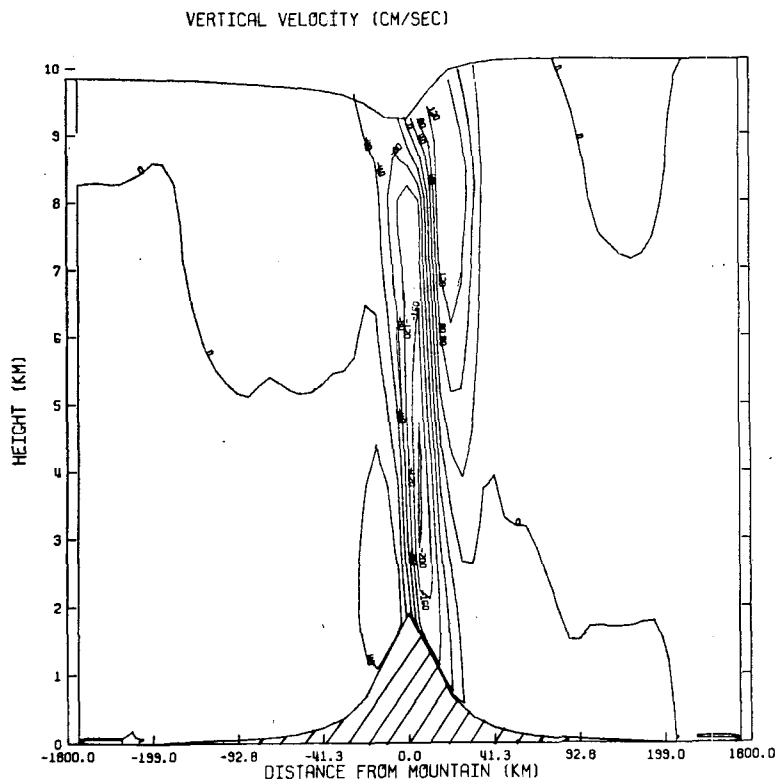


FIG. 7. As in Fig. 4 but with an initial vertical shear of the horizontal wind above the planetary boundary layer.

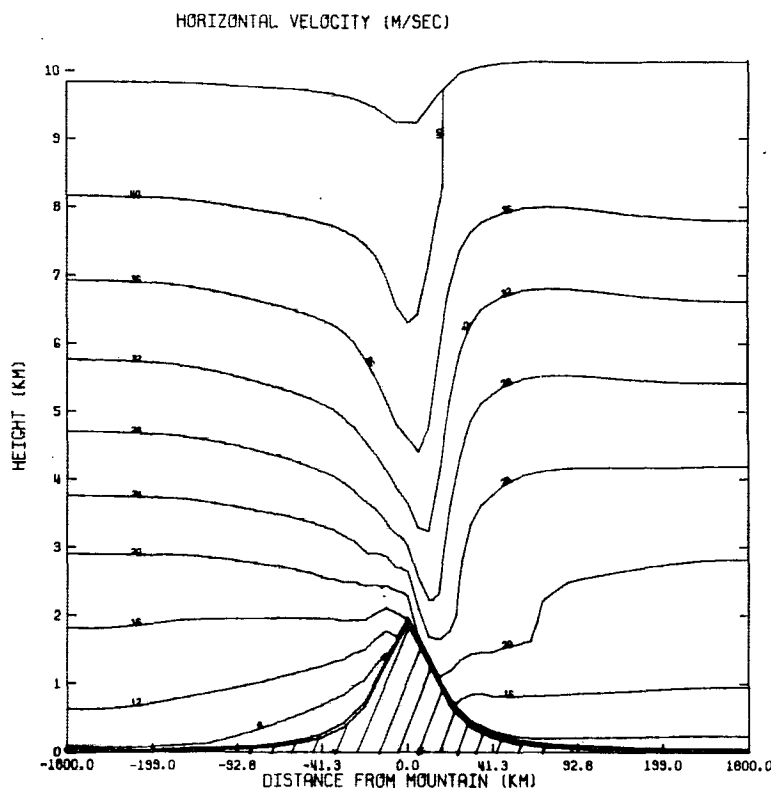


FIG. 8. As in Fig. 1 but with an initial vertical shear of the horizontal wind above the planetary boundary layer.

vicinity of the Rocky Mountains (Danielson and Bleck 1971) and in the United Kingdom at an elevation of about 7 km by Ludlam (1952). A potential temperature field with similar characteristics was observed in the Rocky Mountains on 17 February 1970 (Lilly and Kennedy, 1973, Fig. 1).

## 2) VERTICAL VELOCITIES

The vertical velocity field is shown in Fig. 7 and exhibits the following features.

- (i) A cell of upward motion at low elevation on the windward side with a maximum value of  $0.68 \text{ m s}^{-1}$ .
- (ii) A cell of downward motion above the crest and to the lee of the mountain with a maximum absolute value of  $2.1 \text{ m s}^{-1}$  at an elevation of 4 km.
- (iii) A cell of upward motion in front and above the downward cell with a maximum value of  $1.51 \text{ m s}^{-1}$  at an elevation of 8.5 km, which is about four times greater than in the case without vertical wind shear.

The upward motion cells described above correspond to the locations where cirrus and foehn clouds are often observed (see Section 7b1).

The advantage of using a material surface at the top of the model as opposed to a rigid top is illustrated in

Figs. 4 and 7. With a rigid lid, the solutions are arbitrarily forced by requiring the vertical velocities to approach zero near that level, whereas in the real atmosphere, substantial perturbations of the velocity fields may occur above that level. A material surface can respond more realistically to forcing from below even though the details are not described, since no artificial restraint is applied on the vertical velocity field. An example of the advantage of the material surface is seen by comparing Deaven's (1974) Fig. 53 with our results in Fig. 7. His model extends to 20 km whereas ours reaches only 10 km. Yet, despite the neglect of the upper 10 km, the solutions are quite similar. The vertical motion cell above 10 km predicted by Deaven is well represented by the changes of the material surface in Fig. 7.

## 3) HORIZONTAL VELOCITIES

Fig 8 shows the field of horizontal velocity. As dictated by the vertical velocity field, there is horizontal convergence on the windward side, strong horizontal divergence above and to the lee of the mountain, and strong horizontal convergence on the lee side at high elevation. This strong convergence at high elevations on the lee slope was not found for the non-shear experiment. Similar to the previous experiment, the horizontal velocities have increased to values

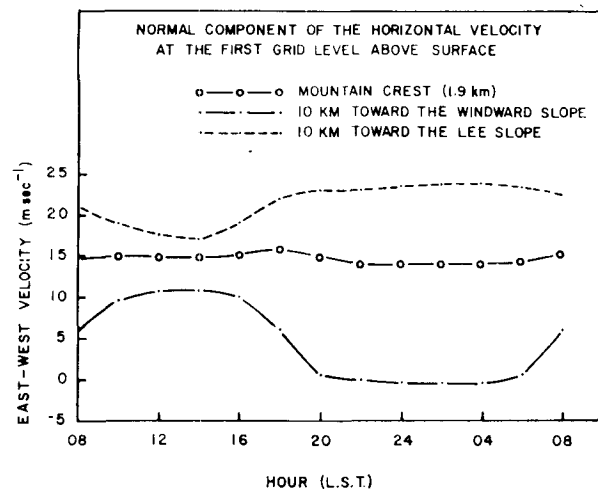


FIG. 9. Hourly output of the east-west component of the horizontal velocity at the first grid level above the surface at three locations: on the mountain crest, 10 km upwind from the crest, and 10 km downwind from the crest.

as high as  $24 \text{ m s}^{-1}$  on the leeward side. The velocities to the lee of the mountain are weaker than on the windward side at high altitudes, agreeing with observations of Lilly and Kennedy (1973, Fig. 2).

### c. Experiment with surface heating

A diurnal temperature wave is imposed on the ground surface after the model was integrated to the steady-state solution described in Section 7a. Due to the heating, the mountain slope and the air in contact with it are warmed during the day relative to the free atmosphere at corresponding levels. This differential heating generates a circulation similar to that of a sea breeze. During the cooling at night, the reverse will be true. Although mountain wind perturbations may be overwhelmed by the synoptic wind system aloft, their influence on the surface wind is well known (see, for example, Defant, 1951).

The form for the diurnal temperature wave (given below) was adopted from Neumann and Mahrer (1974) which was based on a radiative convective model by Kuo (1968). We have reduced the curve's range to  $17^\circ\text{C}$  as a result of the stronger heat fluxes associated with our surface layer formulation. The temperature wave is thus given by

$$\theta(z^*=0, t) = 298 + 8 \sin(15t - 110) + 2.3 \sin(30t + 75) + 0.3 \sin(45t + 66).$$

#### 1) HORIZONTAL VELOCITIES

Fig. 9 shows the hourly output of the east-west component of the horizontal velocity at the first grid level above the surface at three locations: on the mountain crest, 10 km upwind from the crest, and 10 km downwind from the crest. The velocities on the

windward side have intensified relative to experiment A, with a maximum of  $11 \text{ m s}^{-1}$  at about 1300 (all times LST), coinciding with the surface temperature maximum, but then decreasing to relatively slow velocities with an almost constant value of  $-0.5 \text{ m s}^{-1}$  between 2300 and 0400. The wind on the lee slope decreases to a minimum value of  $17.1 \text{ m s}^{-1}$  at 1400 and then intensifies to a maximum of  $24 \text{ m s}^{-1}$  at 0400. Only minor variations of the velocity with time at the crest are observed. Above the lee and windward slopes the winds develop the conventional structure of a countercirculation. Thus, above the windward slope, the velocities decrease during the day and increase at night, while the opposite is true over the lee slope. As one would expect, however, the velocity changes aloft are much weaker than predicted at low levels with a maximum range of about  $2 \text{ m s}^{-1}$  on the windward side and  $1.5 \text{ m s}^{-1}$  on the lee side, in comparison with 11 and  $9.5 \text{ m s}^{-1}$  variations, respectively, near the surface. Observations confirm several features obtained in our calculations. Reference is made to Hoinkes' (1950) data which indicated intensification of wind speed over the windward side in the Austrian Alps, and to Brinkmann's (1974) observation in the lee of the Rocky Mountains which show the strongest winds occurring most frequently between midnight and 1000 LST.

#### 2) VERTICAL VELOCITIES

Fig. 10 and 11 show the vertical velocity fields at 1400 and 0400 respectively. The upward velocities on the windward slope increase from a maximum of  $0.72 \text{ cm s}^{-1}$  to  $0.89 \text{ m s}^{-1}$  during the heating while the intensity of the downward cell decreases from a maximum of  $-2.23 \text{ m s}^{-1}$  to  $-1.95 \text{ m s}^{-1}$ . During the night hours the vertical velocity of the windward slope decreases to  $0.69 \text{ m s}^{-1}$  and increases to a value of  $-2.67 \text{ m s}^{-1}$  on the lee slope. These results agree with what one would expect from a conceptual picture of a mountain circulation, under large-scale flow where the mountain ridge acts as an elevated heat source during the day and as an elevated heat sink at night.

The heating of the mountain crest during the day acts to create a pressure minimum there and to decelerate the flow somewhat as it crosses the ridge. In contrast, during the night, cooling along the crest generates a pressure maximum so that the air flow is additionally accelerated down the leeward slope.

#### 3) HEIGHT OF THE PLANETARY BOUNDARY LAYER

One of the most important results of the present study is illustrated by Fig. 12 where the depth  $z_p$  of the planetary boundary layer, is plotted as a function of distance from the mountain. To our knowledge, this is the first numerical experiment where the depth of the planetary boundary layer is predicted explicitly in a

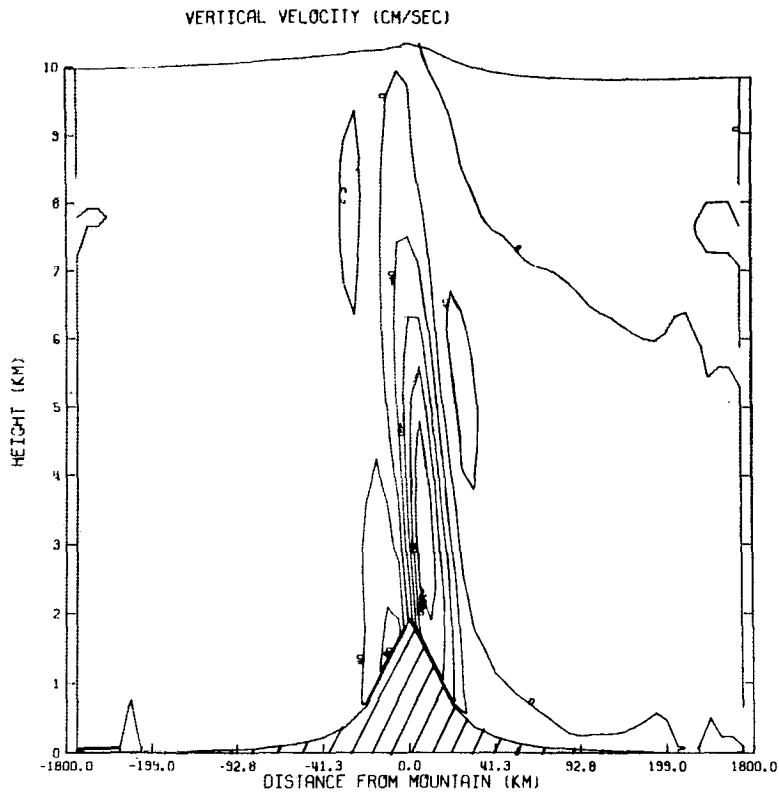


FIG. 10. Vertical velocity field at 1400 LST for the experiment with heating.

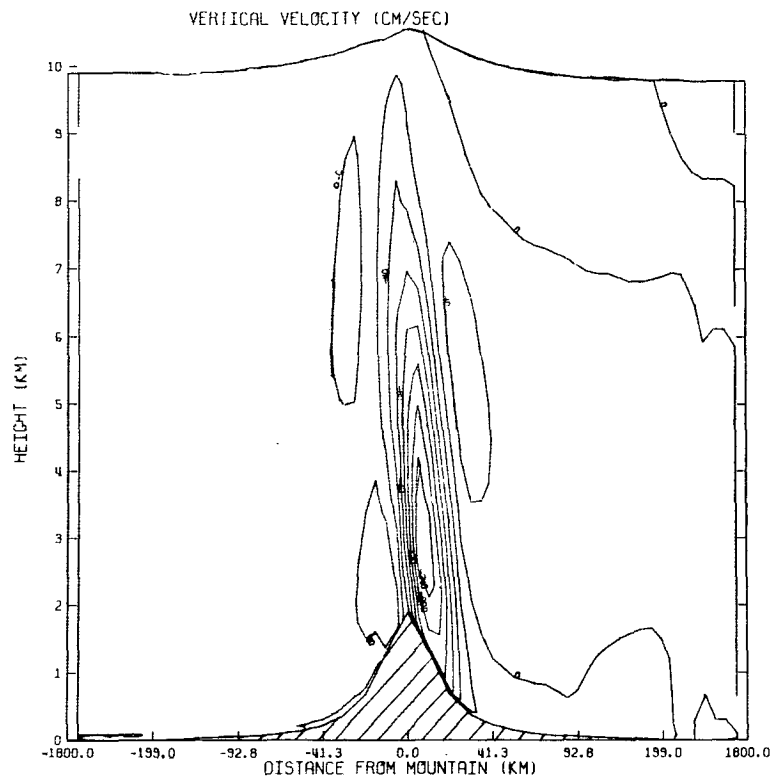


FIG. 11. As in Fig. 10 except for 0400 LST.

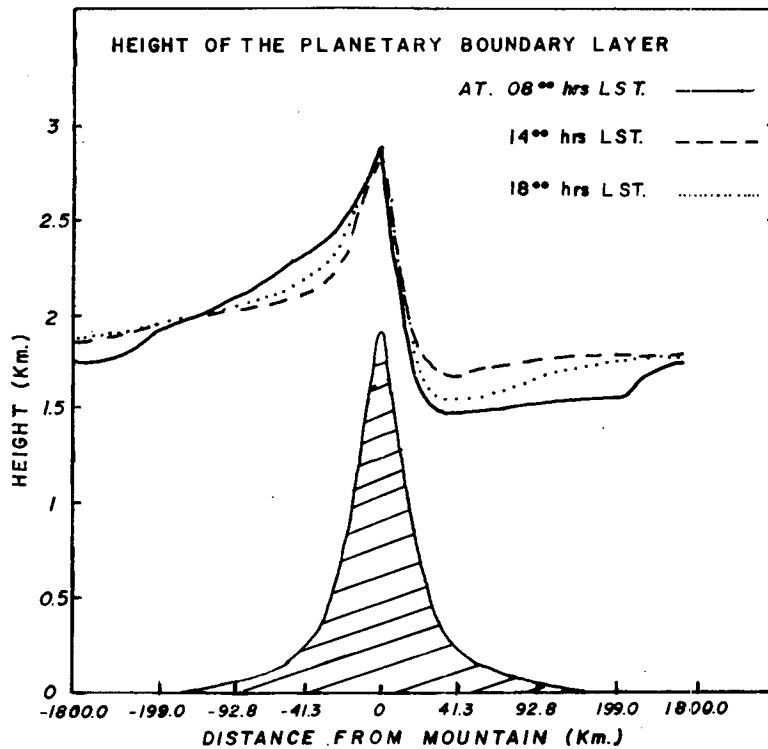


FIG. 12. Height of the planetary boundary layer as a function of the distance from the mountain crest at 0800, 1400 and 1800 LST.

mountain model. At 0800 (the initial time for the heated experiment)  $z_i$  at 30 km downwind from the mountain crest, is about 900 m lower than at an equal distance upwind on the windward side. This is a consequence of the downward motion term in (9), which dominates the other contributions to changes in  $z_i$ . By 1400, or 6 h after surface heating was initiated,  $z_i$  has decreased on the windward side and increased on the lee side, but is still lower on the lee slope by about 600 m. By 1800,  $z_i$  has begun to return to the 0800 position as surface heating diminishes. This result may have a practical application in the location of factories and other pollution sources in a mountain or hilly area. For the situation represented in the experiment, *where the inversion lies above the mountain crest*, the most appropriate place would be on the windward side of mountains where both gaseous and particulate pollutants could be mixed up to higher elevation, thereby decreasing the surface concentrations.

### 8. Conclusion

The ability of the two-dimensional, hydrostatic, primitive equation model discussed in this paper to simulate the air flow over a mountain ridge under simple initial conditions was qualitatively tested against observation and other numerical models. It was found that the results agree quite well with Deaven's and Hovermale's two-dimensional mountain models. More-

over, existing observations for similar atmospheric conditions agree with the salient features as predicted by the model. However, it is clear that our results, based on a hydrostatic model, cannot predict the so-called resonance lee waves which are nonhydrostatic features (see, for example, Vergeiner, 1971, and Lilly and Kennedy, 1973). The effect of surface heating on air flow over a mountain is also studied with the results in qualitative agreement with observations. Work is underway, using the coordinate system presented in this paper, to include general topographic effects, where the forcing function cannot be treated as two-dimensional (such as flow around rather than above a mountain), into the three-dimensional University of Virginia mesoscale model.

*Acknowledgments.* The authors gratefully acknowledge the useful comments by Dr. J. Neumann, Dr. William R. Cotton and Mr. Michael McCumber. Ms. Phyllis Moore performed her usual excellent typing job. This work was supported by the National Science Foundation under Grant GA-43040X.

### APPENDIX

#### List of Symbols

$C_p$	specific heat at constant pressure
$f$	Coriolis parameter
$g$	acceleration of gravity

$i, j$	east-west and vertical grid index
$k_0$	von Kármán's constant
$K_z^{(m)}$	vertical exchange coefficient of momentum
$K_z^{(h)}$	vertical exchange coefficient of heat
$K_H$	horizontal exchange coefficient
$L$	distance from mountain center to the lateral boundaries
$L_*$	Monin-Obukhov stability length divided by $\sigma$ ( $\sigma=15$ )
$P$	pressure
$P_{00}$	reference pressure
$R$	gas constant for dry air
$\bar{s}$	initial height of the material surface
$s$	material surface top of the model
$t$	time
$T$	temperature
$u, v, w$	east-west, north-south and vertical component of velocity
$U_g, V_g$	east-west and north-south geostrophic wind
$u_*$	surface friction velocity
$w^*$	vertical ( $z^*$ ) component of velocity ( $w_i^*, w^*$ evaluated on $z_i$ )
$x, y, z$	Cartesian coordinates
$z^*$	vertical terrain-following coordinate
$z_G$	ground elevation
$z_0$	roughness parameter
$z_i$	depth of the planetary boundary layer
$\alpha$	nondimensional numerical constant in the horizontal exchange coefficient
$\pi$	Exner's function [ $=C_p(P/P_{00})^{R/C_p}$ ]
$\theta$	potential temperature
$\bar{\theta}$	average potential temperature for a vertical layer
$\theta_*$	surface friction temperature
$\theta_s$	surface-potential temperature
$\partial\theta^+/\partial z$	potential temperature gradient immediately above the planetary boundary layer
$\phi_i( \xi )$	nondimensional wind shear
$\Delta t$	time step
$\Delta x, \Delta z^*$	mesh sizes in $x$ and $z^*$ components

## REFERENCES

- Anthes, R. A., and T. T. Warner, 1974: Prediction of mesoscale flows over complex terrain. Tech. Rept. ECOM-5532, Atmos. Sci. Lab., U. S. Army Electronics Command, Fort Monmouth, N.J., 101 pp.
- Brinkmann, W. A. R., 1974: Strong downslope winds at Boulder, Colorado. *Mon. Wea. Rev.*, **102**, 592-602.
- Corby, G. A., and J. S. Sawyer, 1958: The airflow over a ridge: The effects of the upper boundary and high level condition. *Quart. J. Roy. Meteor. Soc.*, **84**, 25-37.
- Danielson, E. F., and R. Bleck, 1970: Tropospheric and stratospheric ducting of stationary mountain lee waves. *J. Atmos. Sci.*, **27**, 758-772.
- Deardorff, J., 1974: Three-dimensional numerical study of the height and mean structure of a heated planetary boundary layer. *Boundary-Layer Meteor.*, **7**, 81-106.
- Deaven, D. G., 1974: A solution for boundary problems in isentropic coordinate models. Ph.D. dissertation, The Pennsylvania State University.
- Defant, F., 1951: Local winds. *Compendium of Meteorology*, Amer. Meteor. Soc., 655-672.
- Foldvik, A., and M. G. Wurtele, 1967: The computation of transient gravity wave. *Geophys. J. Roy. Astron. Soc.*, **13**, 167-185.
- Hoinkes, H., 1950: Föhnentwicklung durch Hohentiefdruckgebiete. *Arch. Meteor. Geophys. Bioklim.*, **A2**, 82-96.
- Hovermale, J. B., 1965: A non-linear treatment of the problem of air flow over mountains. Ph.D. dissertation, The Pennsylvania State University.
- Kuo, H. L., 1968: The thermal interaction between the atmosphere and the earth and propagation of diurnal temperature waves. *J. Atmos. Sci.*, **25**, 680-706.
- Lilly, D. K., and E. J. Zipser, 1972: The front range windstorm of 11 January 1972: A meteorological narrative. *Weatherwise*, **25**, 56-63.
- , and P. J. Kennedy, 1973: Observational of a stationary mountain wave and its associated momentum flux and energy dissipation. *J. Atmos. Sci.*, **30**, 1135-1152.
- Ludlam, F. H., 1952: Orographic cirrus clouds. *Quart. J. Roy. Meteor. Soc.*, **78**, 554-562.
- Neumann, J., and Y. Mahrer, 1974: A theoretical study of the sea and land breezes of circular islands. *J. Atmos. Sci.*, **31**, 2027-2039.
- O'Brien, J. J., 1970: A note on the vertical structure of the eddy exchange coefficient in the planetary boundary layer. *J. Atmos. Sci.*, **27**, 1213-1215.
- Pielke, R. A., 1974a: A three-dimensional numerical model of the sea breezes over south Florida. *Mon. Wea. Rev.*, **102**, 115-139.
- , 1974b: A comparison of three-dimensional and two-dimensional numerical predictions of sea breezes. *J. Atmos. Sci.*, **31**, 1577-1585.
- , and Y. Mahrer, 1975: Representation of the heated planetary boundary layer in mesoscale models with coarse vertical resolution. *J. Atmos. Sci.*, **32**, No. 12 (in press).
- Queney, P., 1948: The problem of air flow over mountains: A summary of theoretical studies. *Bull. Amer. Meteor. Soc.*, **29**, 16-26.
- Richtmyer, R. D., 1957: *Difference Methods for Initial Value Problems*. Interscience, 238 pp.
- Sawyer, J. S., 1960: Numerical calculation of the displacement of a stratified airstream crossing a ridge of small height. *Quart. J. Roy. Meteor. Soc.*, **86**, 326-345.
- Schulman, E. E., 1970: The antarctic circumpolar current. *Proc. 1970 Summer Computer Simulation Conference*, Denver, Colo., 955-961.
- Scorer, R. S., 1949: Theory of waves in the lee of mountains. *Quart. J. Roy. Meteor. Soc.*, **75**, 41-56.
- Shuman, F. G., 1957: Numerical methods in weather prediction: II. Smoothing and filtering. *Mon. Wea. Rev.*, **85**, 357-361.
- Vergeiner, I., 1971: An operational linear lee wave model for arbitrary basic flow and two dimensional topography. *Quart. J. Roy. Meteor. Soc.*, **97**, 30-56.
- Wallington, C. E., 1970: A computing aide to studies of airflow over mountains. *Meteor. Mag.*, **99**, 157-165.